Batteries & Supercaps

Research Article
doi.org/10.1002/batt.202500779

Chemistry
Europe
European Chemical
Societies Publishing

www.batteries-supercaps.org

Hierarchical Porosity Engineering of Birch-Derived Carbons via KOH Activation for High-Performance Aluminum Batteries

Sruthy E S, Menestreau Paul, Gopinathan Manavalan, Nicolas Boulanger, Palanivel Molaiyan, Tao Hu, Ulla Lassi, Christie Thomas Cherian,* Mikael Thyrel, and Shaikshavali Petnikota*

Aluminum batteries (ABs) present a cost-effective, high-energy alternative to lithium-ion systems, owing to aluminum's abundance and high theoretical capacity. Here, it reports the synthesis of birch wood derived carbons (CBWs) via carbonization of sawdust followed by KOH activation and their evaluation as AB cathodes. Two samples CBW14 and CBW16 are prepared using biochar-to-KOH weight ratios of 1:4 and 1:6, respectively. Both materials are highly disordered, predominantly amorphous carbons, exhibiting Brunauer–Emmett–Teller-specific surface areas of $3015\,m^2\,g^{-1}$ (CBW14) and $3306\,m^2\,g^{-1}$ (CBW16). When cycled between 0.01 and 2.2 V at $0.1\,A\,g^{-1}$, CBW14 and CBW16 delivered discharge capacities of 120 and $140\,mAh\,g^{-1}$, respectively. Notably, CBW16 sustained $35\,mAh\,g^{-1}$ at a high rate of $10\,A\,g^{-1}$ and achieved energy densities of $155\,Wh\,kg^{-1}$ at $0.1\,A\,g^{-1}$ and $95\,Wh\,kg^{-1}$ at $1.0\,A\,g^{-1}$. These findings underscore the critical influence of KOH activation parameters on pore architecture and electrochemical performance, pointing the way toward scalable fabrication of efficient carbon cathodes for next-generation aluminum batteries.

1. Introduction

The variable output of renewable energy sources underscores the imperative to pair them with high-performance energy storage systems, among which rechargeable batteries stand out as the leading solution.[1,2] Among different rechargeable batteries, lithium-ion batteries (LIBs) have dominated the portable electronics and electric vehicles markets due to their higher energy density, long cycle life, and low self-discharge rate.[3] Nevertheless, the shortage and uneven distribution of lithium resources and other transition metal precursors, safety issues arising from the thermal runaway, and limited cycle life are a few bottlenecks associated with commercial LIBs. Researchers are exploring various strategies to address these challenges for developing cutting-edge "beyond lithium-ion" batteries, including sodium-ion, magnesium-ion, aluminum-ion, and potassium-ion batteries. Aluminum batteries (ABs) are considered a potential candidate to replace LIBs due to the abundant aluminum reserves, environmental friendliness, affordability, and three-electron transfer mechanism during charging and discharging. Aluminum ($Z = 13$) has the electron configuration [Ne] $3s^2\,3p^1$ and requires 578, 1817, and $2745\,kJ\,mol^{-1}$ to remove its first, second, and third valence electrons, respectively, after which ionization energies rise sharply. The resulting Al^{3+} ion, in its most stable oxidation state, can exchange three electrons per ion in an electrochemical cell, compared to the single-electron transfer of Li^+.[4] As a result, aluminum-ion batteries boast a remarkable theoretical specific capacity of $2980\,mAh\,g^{-1}$ and a volumetric energy density of $8046\,mAh\,cm^{-3}$, outperforming many other metal-based systems.[1,5,6] Moreover, aluminum's ubiquity, as the most abundant metal and the third most abundant element in Earth's crust, translates into lower raw-material costs and enhanced commercial feasibility.[7–12] The slightly smaller ionic radius of Al compared with Li results in a higher charge density, enabling greater charge transfer without imposing additional physical constraints on the electrodes.[4,13] Unlike lithium or sodium, aluminum can be handled in ambient conditions, which enhances safety during large-scale manufacturing and

S. E. S. C. T. Cherian
School of Electronic Systems and Automation
Digital University Kerala
Thiruvananthapuram, India
E-mail: christie.cherian@duk.ac.in

S. E. S. G. Manavalan, M. Thyrel, S. Petnikota
Biomass Technology Centre
Department of Forest Biomaterials and Technology
Swedish University of Agricultural Sciences
SE-90183 Umeå, Sweden
E-mail: shaikshavali.petnikota@slu.se

M. Paul
Public Research University Engineering School
IMT Mines Albi
Albi 81000, France

N. Boulanger
Department of Physics
Umeå University
SE-90187 Umeå, Sweden

P. Molaiyan, T. Hu, U. Lassi
Research Unit of Sustainable Chemistry
University of Oulu
P.O. Box 3000, FI-90014 Oulu, Finland

Batteries & Supercaps

Research Article
doi.org/10.1002/batt.202500779

Chemistry Europe
European Chemical
Societies Publishing

applications.[1] ABs operate via the following reaction mechanism, where the deposition/dissolution of aluminum occurs at the anode (Equation (1)), and intercalation/de-intercalation of $AlCl_4^-$ anions occurs at the cathode (Equation (2)).[7–14]

$$Al + 7AlCl_4^- \leftrightharpoons 4Al_2Cl_7^- + 3e^- \qquad (1)$$

$$C_n[AlCl_4] + e^- \leftrightharpoons C_n + AlCl_4^- \qquad (2)$$

The intercalation behavior of the chloroaluminate ($AlCl_4^-$) anions and the charge storage capacity of ABs are typically constrained by the crystal structure and properties of the host cathode material.[1,15] Until now, different varieties of cathode materials have been investigated in ABs based on ionic liquid electrolyte systems such as carbons,[16–19] sulfides,[20–22] oxides,[23,24] Prussian blue analogs,[25] and polymer materials.[26] Nonetheless, the cathodes used in ABs suffer a few challenges, including poor reversibility, slow kinetics, and difficulties inserting Al-ions into the host material, leading to volumetric changes and structural collapse.[27,28] Graphite has attained significant attention as a cathode material in ABs among carbon-based materials, owing to its remarkable stability and electrical conductivity.[28] Despite that, the interlayer spacing of graphite is too narrow (0.335 nm) to accommodate the large compound anions ($AlCl_4^-$) of size 0.609 nm, eventually leading to huge volume expansion and pulverization issues after a few cycles of charging and discharging.[10–12,29] It is imperative to achieve an optimal balance between the intercalation capacity and structural stability of cathode materials to facilitate the development of high-performance ABs with adequate energy storage capacity and reversibility.[12,27] The introduction of an additional energy storage mechanism, such as surface adsorption, represents a promising strategy to address the inherent limitations of intercalation, thereby enabling the development of ABs with increased charge storage capacity.[12,27] Using activated carbons with high surface area and porous nature as a cathode, can be an appealing strategy that aligns with the above charge storage mechanism. The porous structure is advantageous for storing the chloroaluminate anions on its surface via adsorption/desorption. Besides providing long cycle life, storing chloroaluminate anions on the surface imparts higher gravimetric capacity.[3,12,30] The amorphous nature of activated carbon is particularly advantageous for aluminum-ion batteries because its defect-rich, disordered structure provides abundant active sites for the adsorption of large $AlCl_4^-$ anions. Moreover, the lack of long-range graphitic ordering, combined with a hierarchical micro-mesoporous network, supports efficient ion diffusion and accommodates large anionic species, resulting in improved capacity and rate performance.[3] Nonrenewable carbon sources such as coal, petroleum coke, and other fossil fuels are typically used to mass-produce porous activated carbons. However, this approach is associated with high manufacturing costs and time-consuming processes.[31]

Under these circumstances, the use of biomass-derived materials as precursors for activated carbon synthesis offers a viable strategy to overcome the aforementioned limitations.[32] The inherent structure and composition of biomass or biowaste influence the structural and morphological properties of the resulting carbon nanomaterials.[33–36] In this work, an abundantly available and economically viable biomass-derived precursor was chosen to develop the cathode for ABs, effectively lowering the battery cost while ensuring sustainability and environmental compatibility. Birch trees, when processed in sawmills and pulp industries, produce substantial amounts of waste, which are typically considered low-value byproducts. However, these byproducts possess significant potential for conversion into advanced materials, making them viable candidates for energy storage applications, including batteries and supercapacitors. Besides, wood from European deciduous trees like birch possess features favorable for pore formation, such as inherent heteroatoms. The heteroatoms will be removed during carbonization, creating pores of varied size ranges.[37] The hierarchical porous structure and low tortuosity of wood, characterized by abundant open channels, facilitate efficient electrolyte penetration and ion diffusion. However, untreated biomass carbons generally lack the surface area and porosity necessary for $AlCl_4^-$ storage; an activation process is essential to achieve the hierarchical pore network required for effective Al-ion electrochemical performance.[3,38]

Activated carbon with a high specific surface area and interconnected micro-meso pores was synthesized by tuning the morphological features through the KOH activation method, using birch wood as the precursor. Activation with chemical agents like KOH generates a higher specific surface area and well-defined porosity compared with physical activation.[39] Earlier studies demonstrated that high purity of carbon precursor, exact tuning of the proportion between carbon and KOH, and the activation temperature are the three most important parameters for achieving maximal surface area. These parameters were tuned using reduced graphene oxide (rGO) as a precursor and later tested successfully for variety of biochars.[40–42] In fact, the details of activation method appeared to be more critical than the initial source of carbon (rGO or biochars) as the materials with specific surface area (SSA) exceeding 3000 m^2 g^{-1} and very similar pore size distributions have been produced by the same KOH activation procedure starting from tree cones, bark, birch wood and even spent wood-based mushroom substrate.[43–45] In our earlier work on ABs, a high KOH content with a biochar-to-KOH ratio of 1:8 was utilized to synthesize CBW18 cathodes.[8] While increasing the KOH/carbon ratio can enhance the surface area, excessive activation may not be economically or environmentally viable.[46] However, relying on a single carbon-to-KOH ratio (1:8) does not present the whole scenario of the porosity evolution and its influence on ABs and other applications such as LIBs, dye adsorption, water treatment, etc.[45,47,48] Therefore, a comprehensive study was conducted on the porosity evolution of the CBW samples in relation to their performance in ABs. Three different carbon-to-KOH ratios of 1:4, 1:6, and 1:8 were used to systematically investigate the impact of activation conditions.

This work systematically investigates the effect of KOH activation ratios (1:4, 1:6, and 1:8) on the electrochemical performance of activated carbon derived from a single biomass precursor, sawmill waste of birch wood. While prior studies predominantly focus on achieving high surface area through excessive KOH activation

Batteries & Supercaps

Research Article
doi.org/10.1002/batt.202500779

Chemistry Europe
European Chemical
Societies Publishing

(typically $\geq$ 1:7),[8,49] this study reveals that moderate activation levels (1:4 and 1:6) result in superior electrochemical performance, challenging the conventional paradigm that excessive chemical activation is essential for optimal textural properties. The study highlights a strong relationship between pore architecture and electrochemical behavior, where a balanced micro-mesoporous network facilitates $AlCl_4^-$ ion diffusion and contributes to the high reversible capacity and long-term cycling stability exceeding 5000 cycles. Unlike earlier works that often overlook the impact of pore distribution on long-term performance, this study provides mechanistic insights supported by detailed structural and electrochemical characterization. Moreover, the use of an abundant, low-cost, and renewable feedstock, coupled with a scalable, less chemically intensive activation process, emphasizes the innovation of this work in bridging high-performance energy storage with environmental and process sustainability.

2. Experimental Section

2.1. Materials

The synthesis of electrode materials and the fabrication of aluminum battery (AB) pouch cells were conducted following the procedures outlined in our previous work.[7–12]

2.2. Synthesis of Activated Carbon from Birchwood

Figure 1 shows the schematic representation of the synthesis route. The activated carbon was prepared using a two-step procedure using KOH pellets EMPLURA (Supelco, Merck) as the chemical activating agent. The used synthesis method was similar to the one described by Nordenström et al.,[43] Li et al.[44] and

references therein. Briefly, the precursor was carbonized at 500 °C in a stainless-steel reactor, externally heated by a muffle furnace, while nitrogen gas (99%, AGA) ensured an inert atmosphere during the procedure. The temperature was increased from room temperature to 500 °C at a heating rate of 10 °C min^{-1} and held at this temperature for 1 h. After cooling, the resultant biochars were mixed with KOH for chemical activation with an impregnation weight ratio of 1:4, 1:6, and 1:8. Subsequently, water was added to this mixture of KOH and biochar under constant stirring until KOH was completely dissolved. After stirring for 7 h, the mixture was dried at 90 °C in an oven overnight. The impregnated carbon was pyrolyzed at 900 °C in the reactor described earlier under a nitrogen atmosphere. The temperature was increased from room temperature to 900 °C at a heating rate of 10 °C min^{-1} and held at the final temperature for 1 h. The carbons were then washed with HCl (5 M), followed by deionized water until the wash water achieved a neutral pH. After this, all samples were dried overnight at 105 °C in an oven to obtain the activated carbon powder. The prepared activated carbons were labeled CBW14, CBW16, and CBW18, in which 14, 16, and 18 denote the biochar-to-KOH weight ratios.

2.3. Material Characterization

The elemental mapping and morphology analysis were performed by Schottky field emission scanning electron microscopy (FESEM) using a JEOL JSM-7900F FESEM. The device is equipped with an energy dispersive X-ray spectrometer (EDS) and AZtec software of Oxford Instruments. The analysis was done at 15 kV and a working distance of 10 mm. The surface area of CBW powder was measured through liquid nitrogen physisorption using an Autosorb iQ XR sorptometer (Quantachrome) porosimeter, with results interpreted using the BET and Quenched
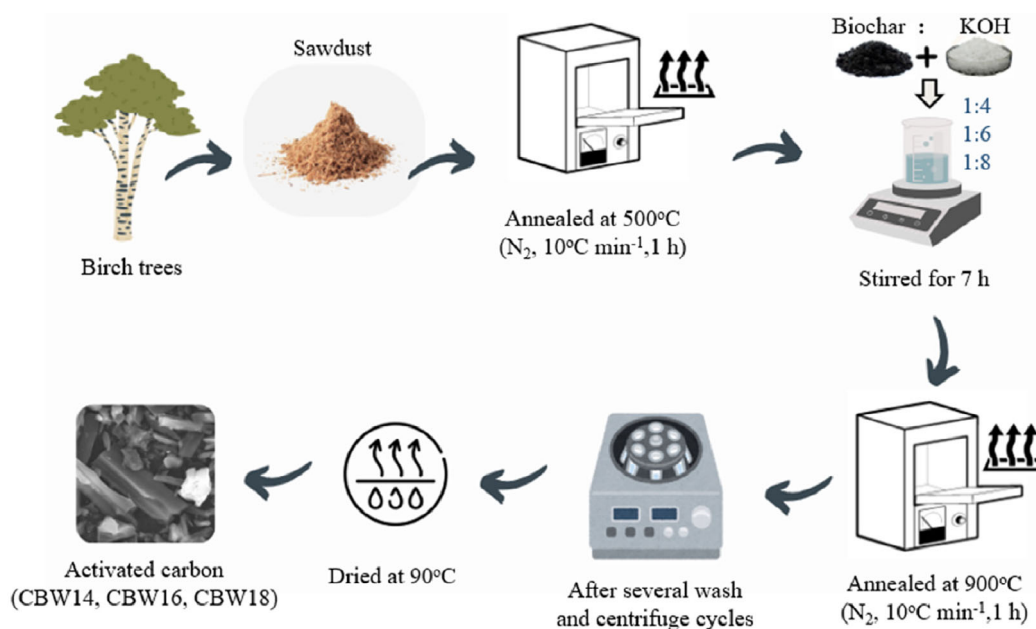

Figure 1. Schematic representation for the synthesis of activated carbons from birch wood.

Batteries & Supercaps

Research Article
doi.org/10.1002/batt.202500779

Chemistry
Europe

European Chemical
Societies Publishing

Solid Density Functional Theory (QSDFT) equilibrium models. Adsorption-desorption isotherms were obtained at −196 °C after degassing the CBWs at 150 °C for 24 h. A 514 nm laser was used to record Raman spectra using a Renishaw Raman spectroscope. On a PANalytical Empyrean X-ray diffractometer fitted with a Cu Kα X-ray tube, X-ray diffraction (XRD) patterns of CBW were captured, spanning a 2θ range of 10–58°. X-ray photoelectron spectroscopy (XPS) was performed with a Thermo Fisher Scientific ESCALAB 250Xi XPS System, detailed instrumentation parameters and analysis conditions were reported elsewhere.[50] Transmission electron microscopy (TEM) imaging was carried out using a JEOL JEM-2200FS EFTEM/STEM. The sample powders were placed on a carbon-coated 200-mesh copper grid. The accelerating voltage and emission current in the measurements were 200 kV and 8–15 μA, respectively. Fourier transform infrared (FT-IR) spectra were acquired using a Bruker IFS 66 v/S spectrometer with dry solid samples diluted in KBr powder before analysis. Thermogravimetric analysis (TGA) was carried out using a TGA/DSC1 STARe device (Metler Toledo, USA). The post-cycling SEM and Raman analyses of the electrodes were carried out in ex situ conditions. The electrodes separated from the pouches in the discharged condition were dried overnight in vacuum at 60 °C. The subsequent SEM imaging was done with an accelerating voltage of 5 kV using Carl Zeiss Merlin field emission scanning electron microscope.
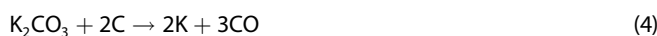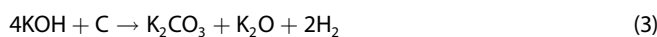
2.4. Electrochemical Characterization, Cell Assembly, and Testing

For assembling ABs, the synthesized CBWs coated on molybdenum (≥99.9%, thickness 0.1 mm, Sigma Aldrich) substrate served as the cathode and aluminum metal (≥99.999%, thickness 0.25 mm, Advent Research Materials Ltd, U.K.) foil as the anode, separated by the Whatman glass microfiber filter. These were placed together inside a pouch, three sides of which were sealed. After vacuum drying at 80 °C overnight inside the glass oven, it was taken inside the Ar-filled glovebox to complete the cell fabrication. To prepare the electrolyte, $AlCl_3$ (99.99%), and 1-Ethyl-3-methylimidazolium chloride, >98% ([EMIM]Cl) were purchased from Sigma–Aldrich and IoLiTec Ionic Liquids Technologies GmbH, Germany, respectively. The pouches were filled with ≈400 μL of 1.3 M $AlCl_3$:[EMIM]Cl electrolyte inside the glovebox, after which the fourth side was sealed. ABs were tested after a minimum relaxation period of 8 h, with all testing conducted at room temperature. The voltage window for testing ABs was 0.01–2.2 V. Cyclic voltammetry (CV) measurements were performed at 1.0 mV s^{-1} using a BioLogic SP-150e potentiostat. Galvanostatic charge–discharge (GCD) measurements were conducted at current densities between 0.1 and 10.0 A g^{-1} using a BioLogic 800 series battery cycler. Electrochemical impedance spectroscopy (EIS) was recorded using a BioLogic SP-150e instrument, employing a 10 mV AC perturbation over the 200 kHz to 0.1 Hz frequency range. The impedance data were obtained at open-circuit voltage (OCV) after 5,701 cycles in the charged-to-2.2 V condition. The data were plotted as Nyquist plots and analyzed by fitting them to an equivalent circuit using ZView2.
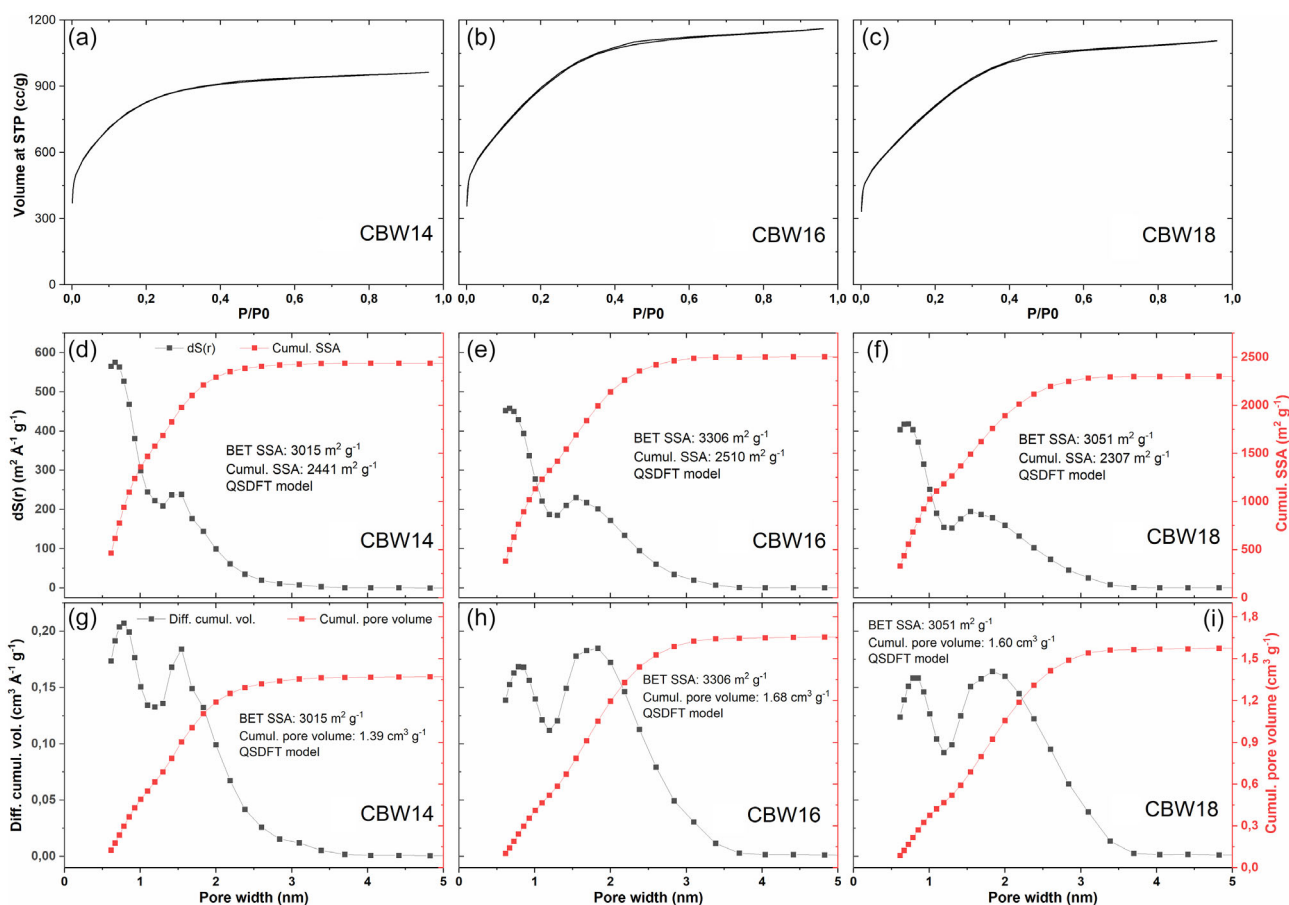
3. Results and Discussion

3.1. Materials Characterization

The specific surface area (SSA), pore area, and volume distributions were obtained from the N_2 adsorption/desorption isotherms using the QSDFT model; results are shown in **Figure 2**. All samples exhibit a combination of type I and type IV isotherms, confirming the presence of both micropores and mesopores, with microporosity being dominant in all cases. CBW16 and CBW18 show relatively higher mesoporosity than CBW14, as indicated by their hysteresis loops. Brunauer–Emmett–Teller (BET) surface area analysis remains the standard for quantifying the accessible specific surface area and pore structure of activated carbon cathodes. A higher BET surface area promotes greater adsorption of $AlCl_4^-$ anions, directly enhancing charge-storage capacity. By comparing BET data across samples activated with varying KOH ratios, one can systematically correlate activation severity with pore size distribution shedding light on how micro- and mesopores develop and contribute to electrochemical performance. However, it is discussed that the cumulative SSA obtained from the DFT model is more accurate.[42–45] Therefore, the SSA obtained from both models is reported. **Table 1** shows a summary of the results from the surface area analysis. The cumulative SSA (2510 m^2 g^{-1}) and the total pore volume (1.680 cm^3 g^{-1}) of the CBW16 are larger than those of the other two carbons (Table 1). The cumulative micropore surface area decreases with increasing C:KOH ratio, i.e., CBW14 (2292 m^2 g^{-1}), CBW16 (2137 m^2 g^{-1}), and CBW18 (1892 m^2 g^{-1}), and the cumulative mesopore area increases, i.e., CBW14 (149 m^2 g^{-1}), CBW16 (373 m^2 g^{-1}), and CBW18 (415 m^2 g^{-1}). The variation in micro-mesoporosity and surface area arises from the differential etching effects associated with varying KOH content in the activated carbon samples (CBW14, CBW16, CBW18). During KOH activation, in the initial stages (400–600 °C), KOH reacts with the carbonaceous biochar and oxygen-containing surface functional groups to form potassium carbonate (K_2CO_3), potassium oxide (K_2O), and hydrogen gas. As the temperature exceeds 700 °C, the formed K_2CO_3 and K_2O serve as primary activating agents; these compounds are reduced by carbon to produce metallic potassium and carbon oxides, which subsequently gasify and escape from the structure. The major reactions involved are described in Equation (3)–(5).

$$4KOH + C \rightarrow K_2CO_3 + K_2O + 2H_2 \tag{3}$$

$$K_2CO_3 + 2C \rightarrow 2K + 3CO \tag{4}$$

$$K_2O + C \rightarrow 2K + CO \tag{5}$$

The intercalation of metallic potassium into the carbon matrix leads to lattice expansion and the generation of pore channels.[51–53] Upon cooling and subsequent washing, potassium and its derivatives are removed, resulting in a porous carbon framework. The evolution of H_2, CO, and CO_2 gases also plays a vital role by physically creating pores within the biochar, thereby enhancing the surface area of the activated carbon.[54,55] Increasing the KOH content

Batteries & Supercaps

Research Article
doi.org/10.1002/batt.202500779

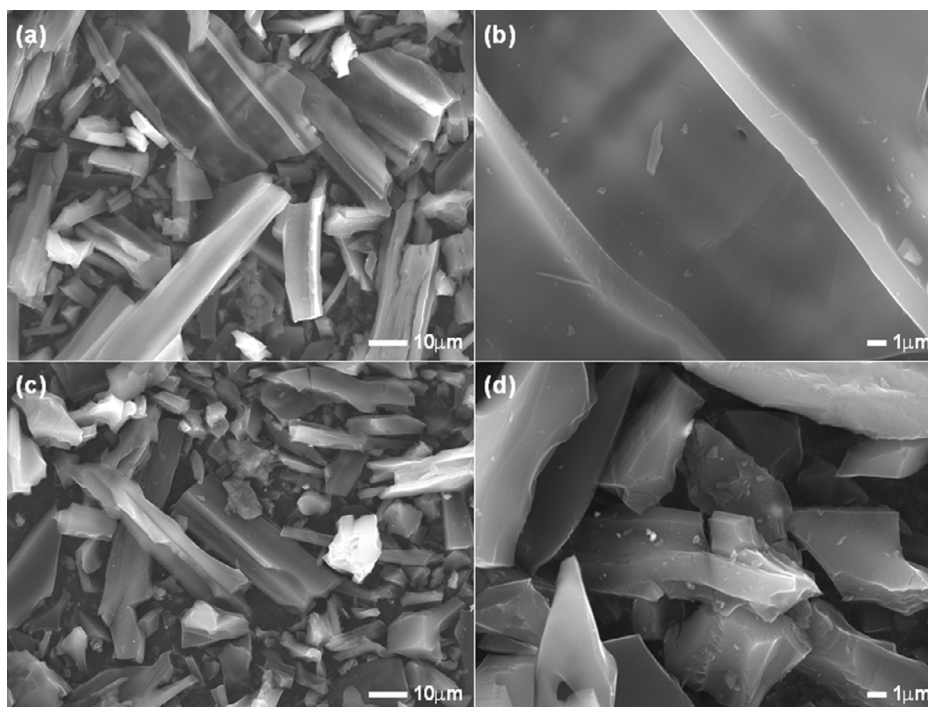**Chemistry**
Europe
European Chemical
Societies Publishing

Figure 2. a–c) Nitrogen adsorption/desorption isotherms, d–f) QSDFT pore size distribution, and g–i) QSDFT pore volume distribution for the birch wood activated carbons.

Table 1. Surface area analysis of the birch wood activated carbons.

Name	CBW14	CBW16	CBW18
BET SSA [$m^2 \ g^{-1}$]	3015	3306	3051
Cumul. SSA [$m^2 \ g^{-1}$]	2441	2510	2307
Micropore SSA [$m^2 \ g^{-1}$]	2292	2137	1892
Micropore SSA [%]	94	85	82
Mesopore SSA [$m^2 \ g^{-1}$]	149	373	415
Mesopore SSA [%]	6	15	18
Total pore volume [$cm^3 \ g^{-1}$]	1.386	1.680	1.603
Micropore volume [$cm^3 \ g^{-1}$]	1.189	1.195	1.056
Micropore volume [%]	86	71	66
Mesopore volume [$cm^3 \ g^{-1}$]	0.197	0.485	0.547
Mesopore volume [%]	14	29	34

promotes the development of a more extensive pore network and higher BET specific surface area (SSA) up to an optimal ratio. In the present study, elevating the ratio from 1:4 to 1:6 markedly enhanced mesoporosity and yielded a maximum SSA of $\approx 3306 \ m^2 \ g^{-1}$. However, further increasing the ratio to 1:8 did not produce additional gains; rather, the cumulative SSA declined. This decline is ascribed to excessive chemical etching at high KOH loadings, which induces collapse of fragile micropore walls and their coalescence into larger mesopores, thereby reducing the overall accessible surface area. Mechanistically, activation proceeds via in situ formation of K_2CO_3 and metallic K, which selectively etch the carbon framework to generate a hierarchical micro-mesoporous architecture.[56] Further structural and chemical characterization was carried out exclusively on CBW14 and CBW16 samples. Sample CBW18 was not re-examined here, as its electrode performance and physicochemical properties have been comprehensively described in our recent work.[8]

The morphology of the CBW14 and CBW16 carbons is analyzed using FESEM and EDS techniques; images are shown in **Figure 3** and Figure S1, Supporting Information, respectively. Individual particles of both the carbons are found in random shapes, whose sizes ranged from several microns to a few nanometers, as seen in Figure 3a–d. The smooth surface finishing features of both the carbon particles suggest their amorphous nature. Particle-size analysis was performed using ImageJ software, and the particle length distribution has been plotted as shown in the Figure S5, Supporting Information. The particle-size distribution follows a lognormal fit, with CBW14 exhibiting $\mu = 3.38074$ and $\sigma = 0.67645$, while CBW16 shows $\mu = 3.18682$ and $\sigma = 0.69424$. Since the characteristic particle size in a

Batteries & Supercaps

Research Article
doi.org/10.1002/batt.202500779

Chemistry Europe
European Chemical
Societies Publishing

Figure 3. Morphology of a,b) CBW14 and c,d) CBW16 carbons seen under FESEM at different magnifications.

lognormal distribution is calculated as $D = e^{\mu}$, CBW14 shows a median particle size of ≈29.4 μm, which is larger than the 24.2 μm obtained for CBW16. The average particle size, calculated using the formula $e^{(\mu+\sigma^2/2)}$, further confirms this trend, with CBW14 exhibiting a larger mean size (≈37.0 μm) compared with CBW16 (≈30.8 μm). CBW16 exhibits a slightly higher σ value (0.69424) than CBW14 (0.67645), indicating a broader distribution with a greater proportion of smaller particles. These statistical results confirm that CBW16 generally comprises smaller particles than CBW14, in agreement with the FESEM observations.[57]

EDS analysis as shown in Table S1, Supporting Information, indicates that CBW14 and CBW16 built in with a carbon content of 97.34 and 96.93 at%, respectively. The respective oxygen contents are found to be 2.66 and 3.07 at%. This elemental oxygen found uniformly distributed all over the individual particles of both CBW samples as seen in Figure S1, Supporting Information. No other elements are detected in the CBW samples. Our previous study on CBW18 samples shows that a further increase in KOH leads to a significant reduction in the particle sizes and an increase in oxygen content; however, the random shapes and amorphous nature of the individual particles persist.[8] The increasing oxygen trend with KOH is also commonly noticed for other KOH-activated biomass-derived carbons as listed in **Table 2**. In general, increasing level of KOH leads to a greater number of residual functional groups such as carboxylates, carbonates, hydroxyl, etc., which eventually contribute to increased oxygen contents.[7,8] Therefore, morphological evolution of CBWs is in tune with KOH activator and in good agreement with the reported similar category of biomass-derived activated carbons.

Figure 4 depicts the HRTEM images of CBW14 and CBW16 individual particles and the corresponding selected area electron diffraction (SAED) patterns. Both the samples exhibit random

shapes with smooth surface finishing and semi-transparent to electron beam as common features as seen in Figure 4a,d. The randomly oriented lattice fringes depicted in Figure 4b,e suggest that both carbons possess a complete amorphous porous structure. Lacking even a short-range ordering strongly indicates that both CBWs are a type of highly disordered carbon. The same is inferred from the corresponding SAED patterns of both CBWs as seen in Figure 4c,f. The diffused ring patterns seen are characteristics of complete amorphous carbons. The TEM inferences of CBW14 and CBW16 are consistent with their SEM morphological features and in good agreement with reported CBW18.[3,8,30]

The surface chemical states of the activated carbon samples CBW14 and CBW16 are examined using X-ray photoelectron spectroscopy (XPS), as shown in **Figure 5**. Both samples exhibit a high carbon content with comparatively low oxygen content (**Table 3**); however, the oxygen contents are slightly higher than those obtained from EDS, indicating an enrichment of oxygen-containing groups at the surface. The survey spectra (Figure S2, Supporting Information) display two dominant peaks at ≈533 eV (O 1s) and 285 eV (C 1s), with no additional elements detected, confirming that the CBW materials consist predominantly of carbon and oxygen. The high-resolution C 1s spectra (Figure 5a,b) can be deconvoluted into five components corresponding to $-CO_3$, O—C=O, C—O—C, C—OH, and C—C moieties. Notably, a pronounced C—C peak is observed, which is attributed to intrinsic structural defects and partially carbonized domains originating from the bio-derived precursor. The O 1s spectra further exhibit contributions from C—O, C—O—C, and C=O species. These oxygen functional groups (OFGs) play an important role in governing the electrode–electrolyte interaction. Their presence increases the surface polarity of the carbon, thereby strengthening electrostatic

Batteries & Supercaps

Research Article
doi.org/10.1002/batt.202500779

Chemistry
Europe
European Chemical
Societies Publishing

Table 2. Electrochemical performance of the current work and various reported cathode materials.

Source	Synthesis method	SSA [$m^2 g^{-1}$]	Current density [$mA g^{-1}$]	Operating potential [V]	Initial DC [$mAh g^{-1}$]	Capacity Retention [$mAh g^{-1}$]/(Cycles)	References
Birch wood (CBW14)	Carbonized at 500 °C under N_2, activated with KOH (1:4), and pyrolyzed at 900 °C under N_2 with a heating rate of 10 °C min^{-1}	3015	100 1000	0.01–2.2 0.01–2.2	101 28	120 (250) 25 (5700)	This work
Birch wood (CBW16)	Carbonized at 500 °C under N_2, activated with KOH (1:6), and pyrolyzed at 900 °C under N_2 with a heating rate of 10 °C min^{-1}	3306	100 1000	0.01–2.2 0.01–2.2	163 46	140 (250) 86 (5700)	This work
Birch wood (CBW18)	Carbonized at 500 °C under N_2, activated with KOH (1:8), and pyrolyzed at 900 °C under N_2 with a heating rate of 10 °C min^{-1}	3029	100 1000	0.01–2.2 0.01–2.2	120 60	115 (300) 70 (2500)	[47,48]
Birch wood	Carbonized at 400 °C under N_2 and activated with 4 wt.% of NaOH under Ar flow at 600–850 °C	3300	283	0.01–2.5	82	69 (40)	[56]
Tar pitch	Tarpitch and KOH (1:4) were heated at 850 °C for 4 h, washed, then heated at 750 °C under N_2 for 2 h	1980	500	0.01–2.25	51	95 (1000)	[56]
Sucrose	Using KIT-6 as a template, sucrose was carbonized in H_2/Ar atmosphere at 900 °C for 3h along with NaOH etching	1185	500	0.01–2.25	82	70 (1000)	[56]
Coconut shell chars	Chemical activation with KOH at 100 °C for 24 h and carbonization at 850 °C under Ar atmosphere for 1h	2686	1000	0.01–2.2	90	81 (1500)	[51–53]
Lignin sulfonate	one-step pyrolysis activation (LS:KOH = 1:2) at 900 °C, with a heating rate of 10 °C min^{-1} for 1 h under N_2 atmosphere	1708	100 1000	0.01–2.2 0.01–2.2	91 64	66 (500) 74 (6700)	[57]
Human hair	Pyrolyzed dried hair in Ar atmosphere at 300 °C for 90 minutes and mixed with NaOH (1:2 mass ratio), followed by carbonization at 750 °C for 3 h under Ar	–	50	0.2–2.45	103	100 (50)	[58–60]
Pomegranate peel	Carbonized at 900 °C for 1 h at a heating rate of 5 °C min^{-1} followed by ball milling for 5 min	81.38	200	0.01–2.4	150	125 (200)	[61–63]

interactions with ionic species and enhancing ion accessibility within the pore structure. Experimental studies have shown that OFGs improve the interfacial affinity and spreading behavior of ionic-liquid electrolytes on carbonaceous surfaces, a phenomenon directly relevant to the $AlCl_3$–EMImCl medium used in aluminum-ion batteries. Enhanced interfacial wetting facilitates deeper electrolyte penetration into the hierarchical pore network, promoting more efficient $AlCl_4^-$ adsorption and reducing interfacial resistance. In addition, carbonyl- and carboxyl-type OFGs may contribute minor pseudocapacitive charge storage through reversible quinone/hydroquinone-type redox transitions.[3,8,38,58–60]

Figure 6a presents the XRD patterns of the CBW14 and CBW16 samples. Both the patterns missing characteristic graphitic (002) peak at 26.5° confirms that the carbons are not crystalline.[8] A broadened hump-like residual diffraction peak is found around 44° for CBW14. The peak corresponding to the (100) plane of graphitic structures indicates the in-plane order of carbon layers; however, its weak intensity suggests a high degree of disorder and small crystallite sizes.[7,8] Notably, with increasing KOH content, the 100 peak broadens further and becomes less defined, highlighting an enhanced degree of structural disorder and the amorphous nature of CBW16. These patterns collectively indicate an amorphous structure of the synthesized

carbon materials, which is consistent with diffused ring SAED patterns seen in TEM analysis. The structural disorder of the activated carbon samples is analyzed using Raman spectroscopy. The Raman spectra of CBW14 and CBW16, as depicted in Figure 6b, reveal two prominent peaks at ≈1350 and 1590 cm^{-1}, corresponding to the D and G bands, respectively.[7,8] The intensity ratio of these bands (I_D/I_G) is a key parameter for assessing the degree of disorder in the activated carbon materials.[7,9–11,61–63] The I_D/I_G ratio was determined to be 0.91 for CBW14 and 0.99 for CBW16. An increase in the amount of KOH resulted in a slight rise in the I_D/I_G ratio, indicating an increased degree of disorder and reduced graphitization. The noticed disorder is extremely high when compared with commercial graphite that bears an I_D/I_G ratio of 0.05 only.[9,63] The complete absence of 2D band around 2700 cm^{-1} confirm lack of graphitic planes stacking order along c-direction.[9,63] These findings are in tune with the XRD results, further supporting the structural characteristics of the materials. TGA results for CBW14 and CBW16 those recorded in air atmosphere with a heating rate of 5 °C min^{-1} are shown in Figure 6c,d, respectively. The analysis showed that the ash content of both carbons is very low (around 0.5 wt%). The negligible amount of retained ash content classifies CBWs as exceptionally high quality when compared with other similar birch wood-derived activated carbons with ash content up to 7.4 wt%.[45]
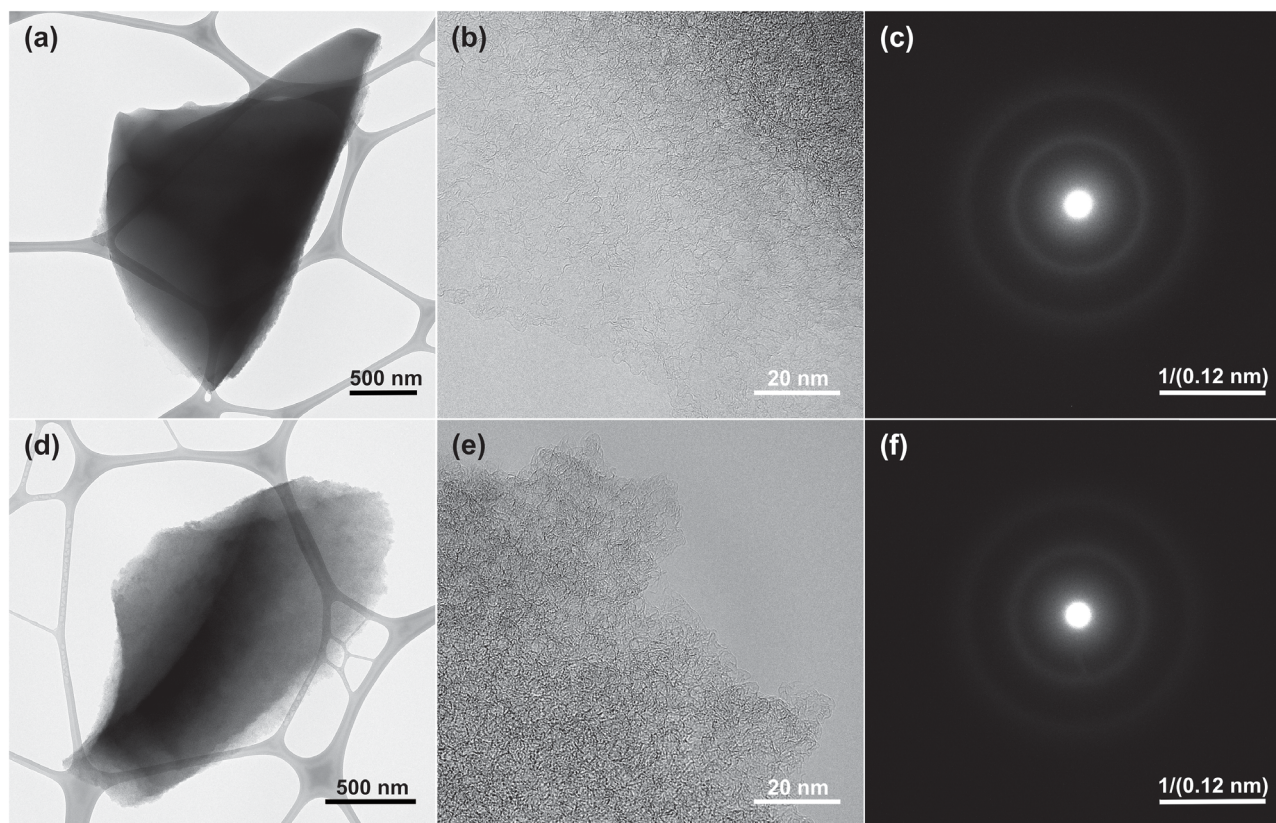
Batteries & Supercaps

Research Article
doi.org/10.1002/batt.202500779

Chemistry Europe
European Chemical
Societies Publishing

Figure 4. TEM images and SAED patterns of a–c) CBW14 and d–f) CBW16.

3.2. Electrochemical Characterization

The electrochemical performance of the activated carbons CBW14 and CBW16 are investigated in a half-cell configuration with Al metal as an anode. The electrochemical behaviors of the developed non-aqueous AB pouch cells were characterized by galvanostatic charge–discharge (GCD) tests, cyclic voltammetry (CV), and rate capability tests. **Figure 7**a,b shows the CV tests of the activated carbons CBW14 and CBW16, respectively. The CV curves demonstrate a charge storage mechanism that is pseudocapacitive in behavior. The cathodic and anodic currents exhibited a quasi-rectangular shape with no oxidation or reduction peaks associated with intercalation/deintercalation mechanisms. The CV curve of CBW16 exhibits a comparatively larger area than CBW14, indicating its greater electrochemical performance. The quasi-rectangular shape of both samples suggests a highly reversible adsorption/desorption of the chloroaluminate ions to the surface of the activated carbons.[3,7,8] The overlapping nature of the CV curves at a constant current highlights the stable performance of the electrodes. Unlike graphite-like materials and multilayered graphene cathodes, where the intercalation phenomenon is predominant, the $AlCl_4^-$ anions are stored via surface-related mechanisms in the synthesized activated carbons as described in Equation (1), (2).[3,7,8,14,64] This can be further confirmed by the GCD profiles recorded with current density of 0.1 A g^{-1} as illustrated in Figure 7c,d. The charge–discharge curve does not exhibit any obvious plateau, affirming that surface adsorption/desorption is the dominant charge storage mechanism. At a current density of 0.1 A g^{-1}, CBW16 exhibits a higher specific capacity of 140 mAh g^{-1} (Figure 7e), whereas CBW14 exhibits 120 mAh g^{-1} (Figure 7f). As cycling progresses, the curves for CBW16 and CBW14 tend to overlap, indicating their relatively better stability, as demonstrated by the CV curves. CBW16 exhibits a more pronounced slanted discharge plateau in the GCD profile due to its higher mesopore content, where faster electrolyte penetration and quicker activation of accessible adsorption sites contribute to the enhanced first-cycle capacity. The first cycle GCD and CV curves are different and exhibit poor performance compared to the subsequent cycles due to electrode activation and electrolyte percolation. In the first cycle, ions might be unable to access the electrode due to low wetting of the electrolyte. For CBW16, the discharge capacity begins at ≈163 mAh g^{-1} and stabilizes around 140 mAh g^{-1}, whereas for CBW14, it starts at about 101 mAh g^{-1} and stabilizes near 120 mAh g^{-1} at 0.1 A g^{-1} (after 250 cycles). Figure 7e,f denotes the cyclic stability of CBW samples evaluated at 0.1 A g^{-1} up to 250 cycles. The coulombic efficiency is maintained close to 100% after the initial few cycles. This implies that the charge–discharge processes are highly reversible without profound side reactions and loss of chloroaluminate anions.

Figure 8a,b illustrates the GCD profiles of CBW14 and CBW16, respectively, at a current density of 1.0 A g^{-1}. Even at high current density, the materials exhibited a similar curve as 0.1 A g^{-1} cycling without any plateau, asserting that the charge storage occurs
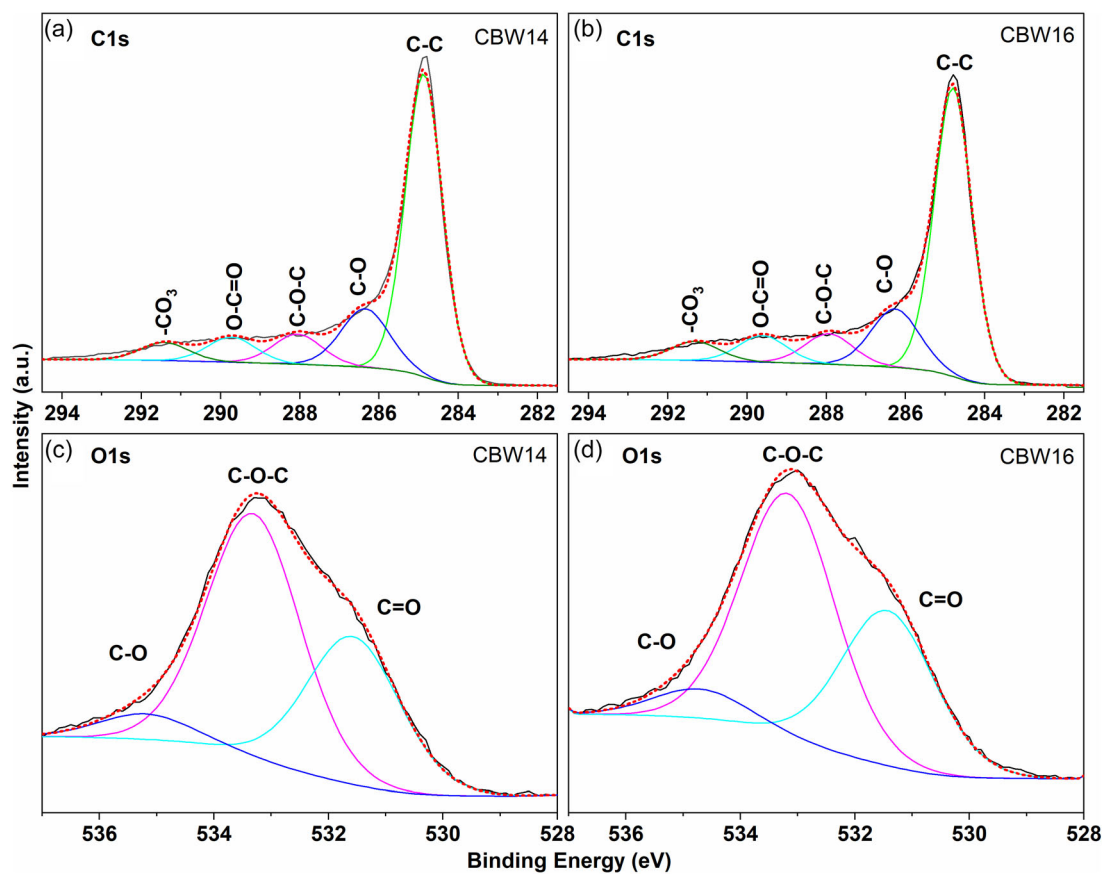
Batteries & Supercaps

Research Article
doi.org/10.1002/batt.202500779

Chemistry
Europe
European Chemical
Societies Publishing

Figure 5. XPS high resolution C1s and O1s spectra of a,b) CBW14 and c,d) CBW16.

Table 3. XPS surface elemental composition of the activated carbons.

Sample	CBW14		CBW16	
Bonding	Position [eV]	at%	Position [eV]	at%
C—C	284.87	59.99	284.8	59.17
C—OH	286.35	15.26	286.26	15.5
C—O—C	288.06	7.85	287.94	8.08
O—C=O	289.73	6.55	289.6	7.04
CO$_3$	291.42	4.74	291.31	5.03
Total	–	94.39	–	94.82
O=C	531.57	1.99	531.43	1.88
C—O—C	533.31	3.28	533.16	2.95
O—C	535.20	0.34	534.71	0.35
Total	–	5.61	–	5.18

through surface-related processes rather than intercalation. In both electrodes, the capacity increases consistently up to 3000 cycles, after which it begins to decline in the case of CBW14 while stable performance is noticed for CBW16. However, the capacity drop in CBW14 is significantly pronounced compared to CBW16. The high extent of microporosity about 86% and larger particle sizes are plausible reasons behind the drastic capacity decline of CBW14. Insertion of larger AlCl$_4^-$ anions into CBW14 seems to induce a higher volume expansion level, which

leads to electrochemical rupturing and pulverization of the electrode matrix that eventually contributes to the capacity fading and deteriorates the cyclic performance.[3,65] The continuous structural collapse induced by electrochemical stress may have progressively diminished the accessible diffusion channels and active sites for charge carriers, i.e., AlCl$_4^-$ anions, and thus results in the observed continuous capacity loss of CBW14. Nonetheless, decomposition of electrolyte species is most unlikely to be responsible for the capacity degradation as higher CE values around 100% (before structural changes initiated) rule out the possibility of such side reactions.[11,66] On the other hand, CBW16 mitigated all these issues owing to its increased mesoporosity (29%) than CBW14 (14%). In general, higher mesoporosity, greater SSA, and larger pore volumes are favorable for achieving better performance as AB cathode material.[3,12] It is worth noticing that CBW16 performed better than its counterparts for being the one that contains the highest SSA (3306 m^2 g^{-1}) and the largest total pore volume (1.68 cm^3 g^{-1}) as furnished in Table 1. At a current density of 1.0 A g^{-1}, CBW14 loses 58% of its initial capacity (Figure 8c), whereas CBW16 shows an 11% increase in capacity after 5700 cycles (Figure 8d). The capacity of 86 mAh g^{-1} for CBW16 highlights its superior performance over CBW14, whose capacity is 25 mAh g^{-1} only.

Figure 8e,f exhibits the rate capability performance of the CBW14 and CBW16 cathodes, respectively, at different current

Batteries & Supercaps

Research Article
doi.org/10.1002/batt.202500779

**Chemistry
Europe**
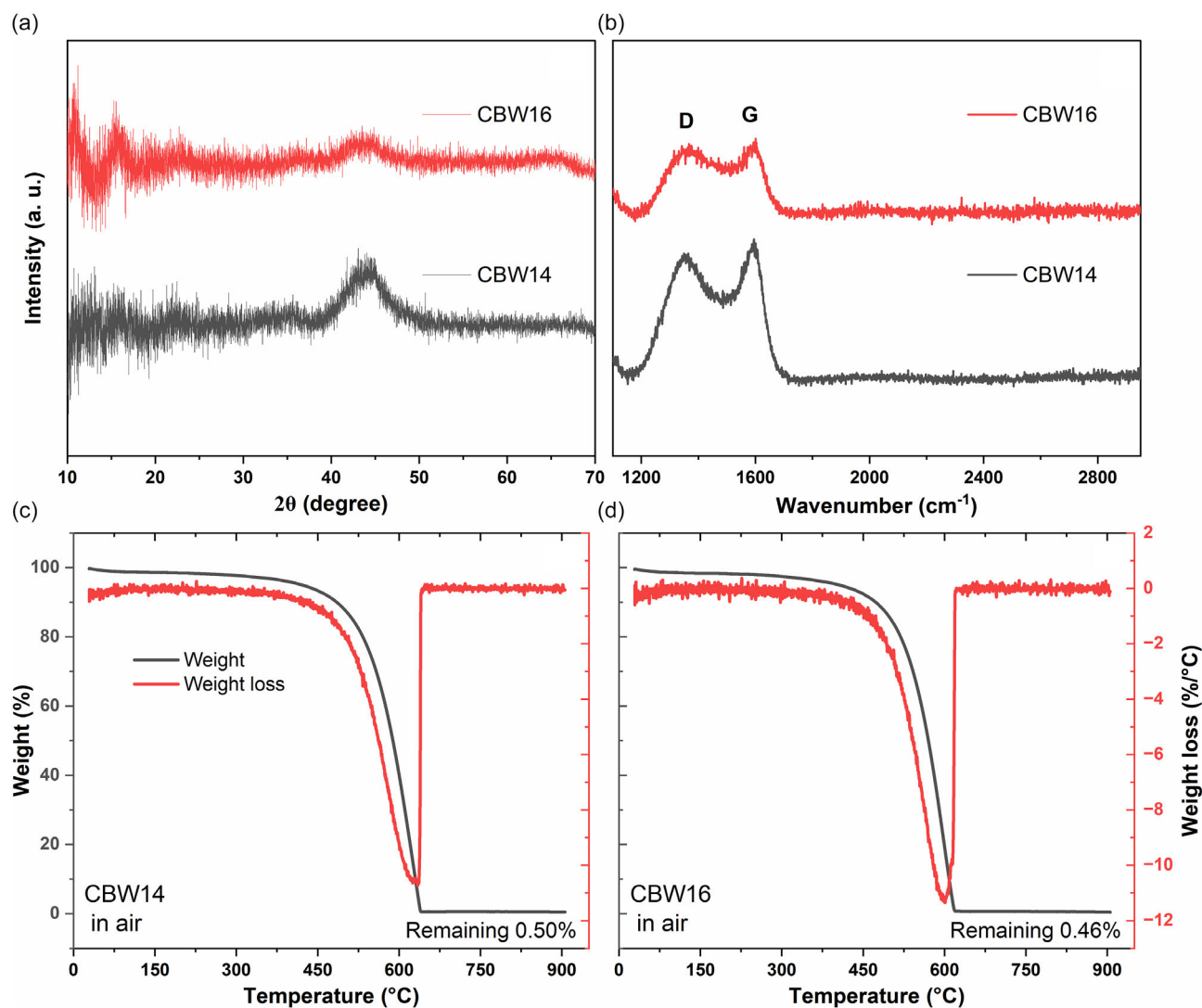European Chemical
Societies Publishing

Figure 6. a) XRD, b) Raman, and c,d) TGA analyses of the CBW14 and CBW16.

rates. CBW16 displayed superior rate capability by delivering discharge capacities of 84, 66, 60, 57, 53, 35, 91, and 135 mAh g^{-1} at 1.0, 2.0, 3.0, 4.0, 5.0, 10.0, 1.0, and 0.1 A g^{-1}, respectively (Figure 8f). The specific capacity for both the activated carbons decreased with increasing current density due to the lack of efficient ionic diffusion within a short time interval. Even at a very high current density of 10.0 A g^{-1}, CBW16 exhibited remarkable electrochemical performance, achieving a capacity of 35 mAh g^{-1}. This is superior to the reported cathode materials, such as commercially available ordered mesoporous frameworks, which gave a superior rate of 30.5 mAh g^{-1} at 5.0 A g^{-1}.[64] In contrast, CBW14 showed poor rate capability and capacity started to decline drastically at an early stage, say from the 750th cycle onwards, when current density switched from 1.0 to 0.1 A g^{-1} as seen in Figure 8e. Overall, CBW16 seems to have balanced micro-mesoporosity to yield the best AB performance and is useful for practical applications compared to other CBWs and its similar category of other biomass-derived activated carbons.

The energy density (E_d) of the activated carbon cathodes was calculated using the relation.

$$E_d = \Delta V \times C_s \tag{6}$$

$$\Delta V = \frac{(V_{max} + V_{min})}{2} \tag{7}$$

where ΔV represents the average voltage, V_{max} the upper voltage limit (2.2 V), V_{min} the lower voltage limit (0.01 V), and Cs is the specific capacity (Ah kg^{-1}), yielding energy density in Wh kg^{-1}. The developed activated carbon, CBW16, demonstrated a superior energy density of 95 Wh kg^{-1} at 1000 mA g^{-1} and 155 Wh kg^{-1} at 100 mA g^{-1}, outperforming most existing activated carbon cathodes, including the birch wood-derived activated carbon synthesized with a carbon to KOH ratio of 1:8.[8] These energy density values surpass the expensive synthetic carbon cathodes such as commercial graphene and CVD graphene foams.[10,14] Table 2 provides a detailed comparative analysis of the electrochemical performance of the current work and various
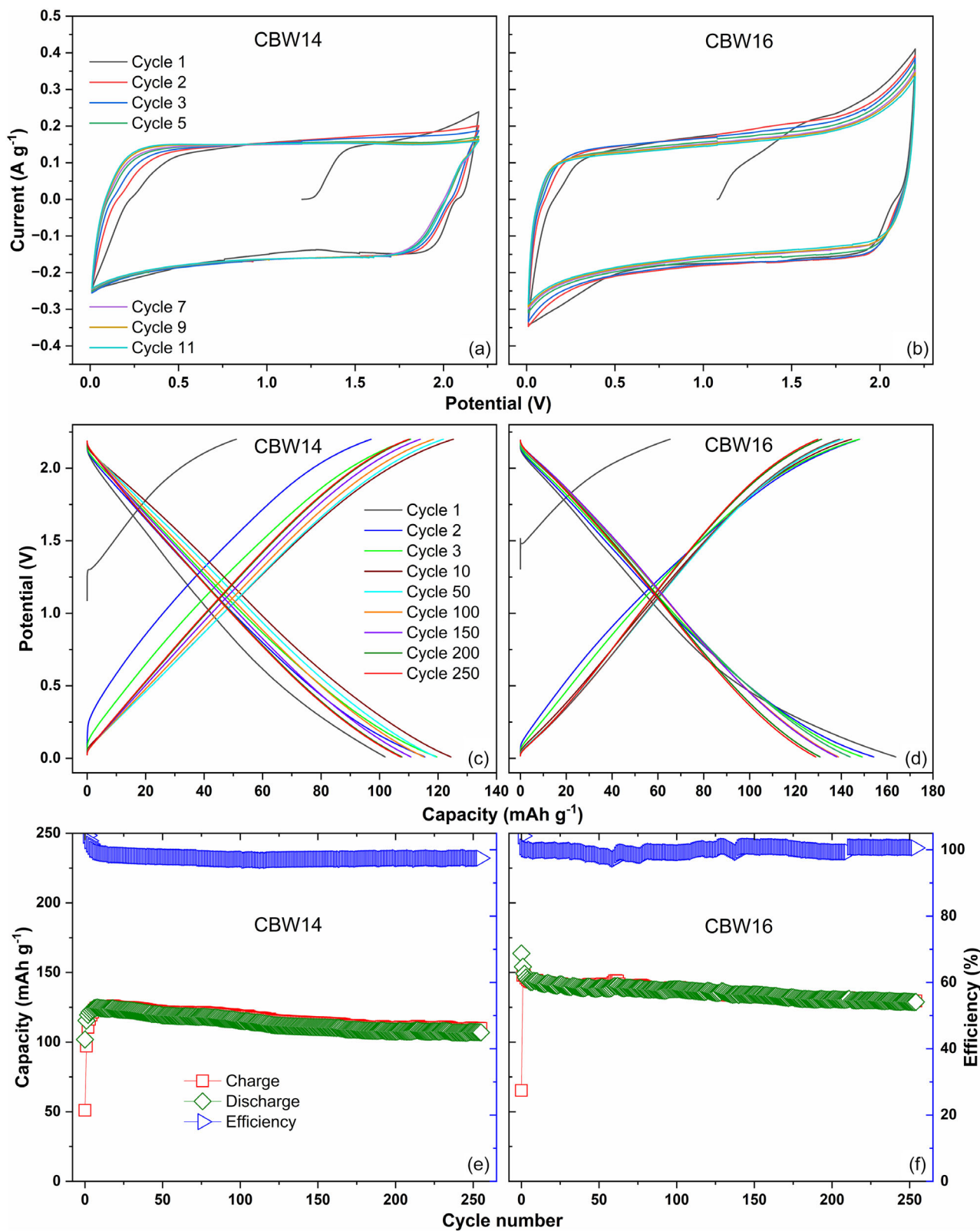
Figure 7. CV for a) CBW14 and b) CBW16 at 1 mV s^{-1} scan rate. Electrochemical features of CBW samples c,d) charge and e,f) discharge cycling performance at 0.1 A g^{-1} current rate.
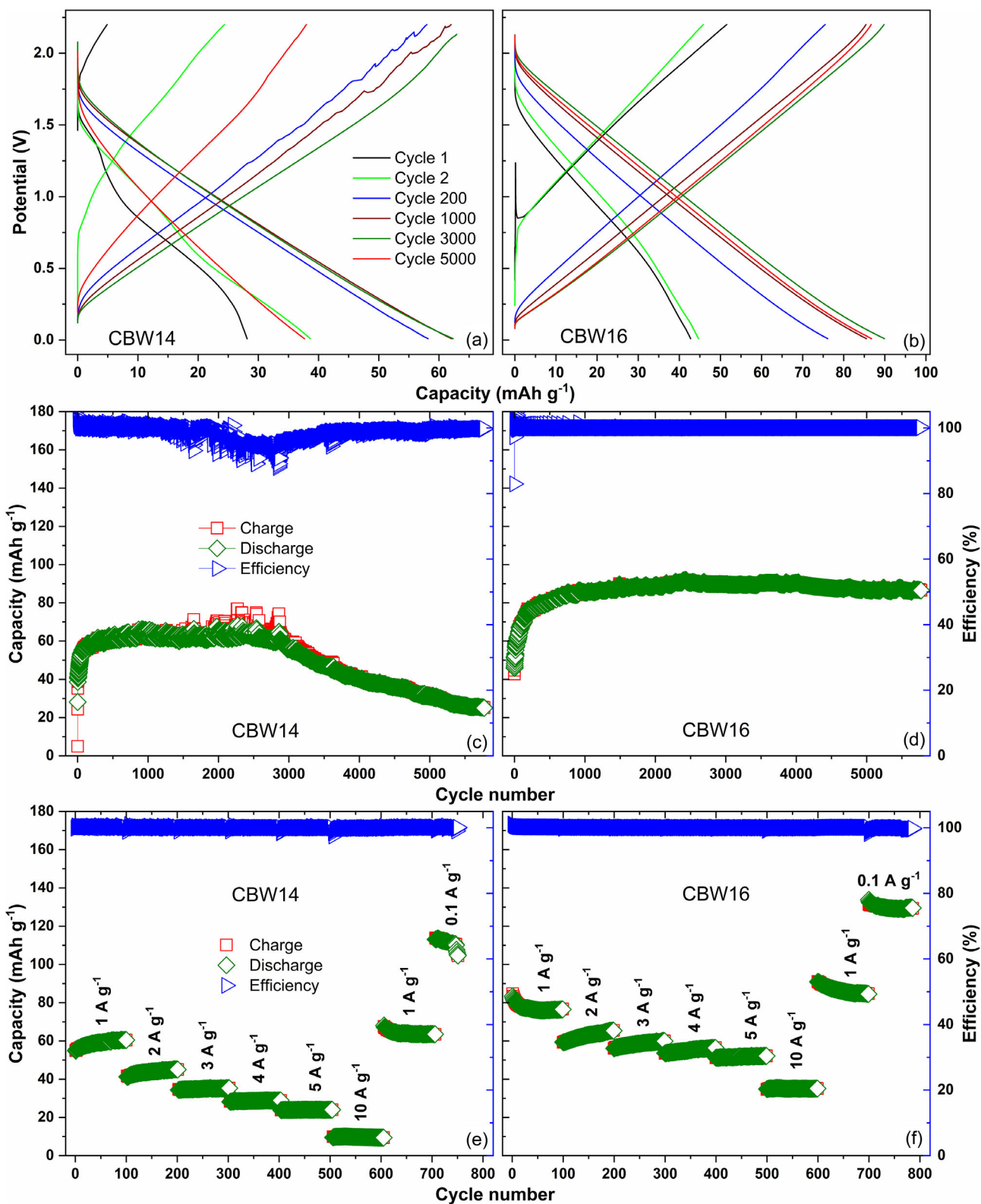
Figure 8. Charge–discharge, cycling features at 1.0 A g^{-1} current rate and rate capabilities of a,c,e) CBW14 and b,d,f) CBW16.

reported similar class of cathode materials. The performance of the developed activated carbon CBW16 surpassed that of various biomass-derived carbon cathodes, as shown in Table 2. For example, lignin sulfonate-derived cathode demonstrated an initial capacity of 64 mAh g^{-1} at a current density of 1 A g^{-1} that ended up at 74 mAh g^{-1} after 6700 cycles.[7] In contrast, CBW16

Batteries & Supercaps

Research Article
doi.org/10.1002/batt.202500779

Chemistry Europe
European Chemical
Societies Publishing

exhibited a lower initial discharge capacity of 46 mAh g^{-1} at 1 A g^{-1}; its capacity increased over time and stabilized at 86 mAh g^{-1} even after 5700 cycles, highlighting its superior long-term stability (Figure 8d).

A comparative assessment of various activated carbon cathodes is reported in Table 2. Compared with its counterparts, CBW16 delivers markedly superior cycling stability as seen in Figure 8 and S3, Supporting Information. After 5700 cycles it retains 86 mAh g^{-1}, whereas CBW14 fall to 25 mAh g^{-1}. On the other hand, CBW18 too retained lesser capacity of 70 mAh g^{-1} after 2500 cycles (Figure S3f, Supporting Information). Moreover, CBW16 outperforms a broad spectrum of both biomass-derived and synthetic carbon cathodes reported in the literature, underscoring its exceptional long-term durability in aluminum-ion cells. For instance, NaOH-activated birch wood with comparable surface area retained only 69 mAh g^{-1} over 40 cycles, while tar pitch and sucrose-derived carbons exhibited inferior capacities of 51 mAh g^{-1} and 82 mAh g^{-1} respectively, after 1000 cycles, showing limited long-term stability. Similarly, coconut shell-based activated carbon retained 81 mAh g^{-1} after 1500 cycles, and lignin sulfonate-derived carbon, though stable over 6700 cycles, exhibited much lower initial capacity. Other sources, such as human hair and pomegranate peel, offered promising short-term performance or high initial capacities but lacked sustained retention over extended cycling. In contrast, CBW16 delivers a compelling combination of high capacity, excellent retention, and rate capability, validating the advantages of a finely tuned activation process and pore architecture optimization.

The EIS results showed in Figure S6, Supporting Information, and the fitted parameters summarized in Table S2, Supporting Information, clearly distinguish the cycling behavior of CBW14 and CBW16. At OCV, both electrodes exhibit high R_{ct} (resistance to charge transfer) and R_b (bulk resistance)[8,11] values, indicating limited initial electrolyte wetting and restricted ion transport, with CBW14 showing a significantly higher R_b than CBW16, suggesting poorer pore accessibility. After 5700 cycles, both electrodes undergo activation, as reflected in the substantial reduction in R_{ct} and R_b; however, CBW16 attains a markedly lower final R_{ct} than CBW14, indicating more efficient interfacial kinetics and better retention of electrochemically active sites. Although R_b
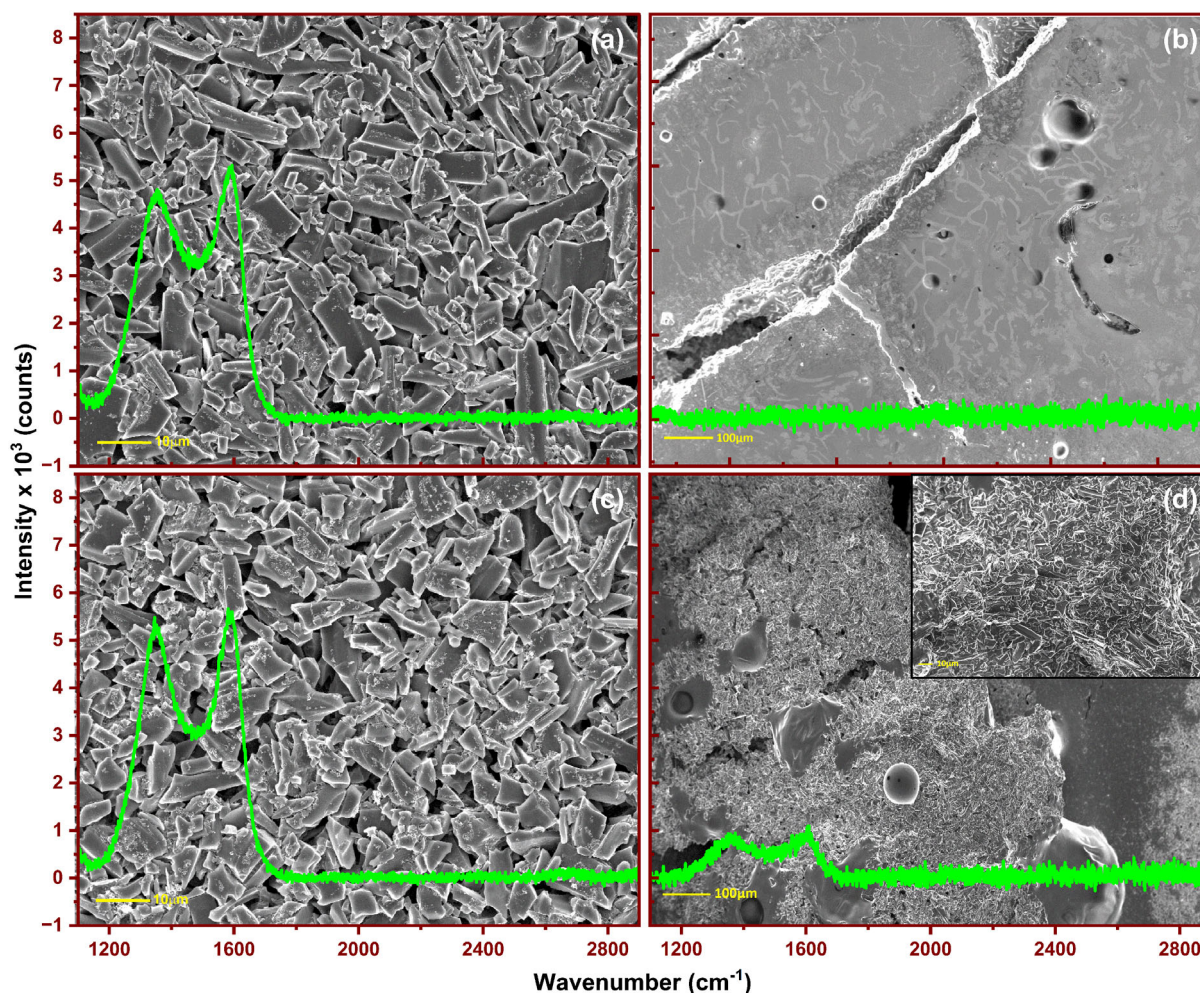
Figure 9. Raman and SEM analyses a) CBW14 fresh electrode, b) CBW14 electrode after 5700 cycles, c) CBW16 fresh electrode, and d) CBW16 electrode after 5700 cycles (inset: magnified view, scale bar −10 μm).

Batteries & Supercaps

Research Article
doi.org/10.1002/batt.202500779

Chemistry Europe
European Chemical
Societies Publishing

converges to similar values for both samples, the increase in R_e (ohmic resistance)[8,11] for each electrode reflects expected long-term cycling effects. The CPE_{dl} (constant phase element)[8,11] parameters further underscore the superior structural stability of CBW16. Its CPE exponent (α) increases from 0.79 to 0.84, demonstrating a shift toward more ideal and uniform double-layer behavior after prolonged cycling. In contrast, CBW14 exhibits a significant decrease in α (0.83 → 0.56), consistent with the rise in surface heterogeneity, pore blockage, and structural degradation as seen in Figure 9 an Figure S4, Supporting Information. These impedance trends correlate with the electrochemical performance, where CBW16 exhibits higher capacity retention and better long-term cycling stability compared with CBW14.

SEM and Raman characterizations of pre- and post-cycled electrodes (**Figure 9**) highlight the contrasting structural stability of CBW14 and CBW16 electrodes. The fresh CBW14 electrode (Figure 9a) exhibits a porous activated carbon framework with irregular rod-like structures. After 5700 cycles, these features are no longer visible (Figure 9b), indicating electrochemical rupturing of the individual carbon particles and subsequent formation of the continuous electrode matrix. Moreover, Raman spectra of the cycled CBW14 electrode show complete suppression of the D ($\approx$1350 cm^{-1}) and G ($\approx$1585 cm^{-1}) bands, confirming the loss of graphitic domains and the transition to an amorphous state. The SEM image of CBW14 electrode after the rate capability test (Figure 8e), as shown in Figure S4a, Supporting Information, and corresponding Raman spectrum in Figure S4b, Supporting Information, further confirm the total amorphisation of the electrode matrix. In contrast, CBW16 exhibits remarkable structural resilience as seen in Figure 9d. The irregularly shaped carbon architectures and interconnected porous network (Figure 9c) in the pristine CBW16 electrode are largely retained even after 5700 cycles (Figure 9d), while the Raman spectra continue to exhibit pronounced D and G bands, indicative of the structural stability of turbostratic domains and defect-enriched sites crucial for reversible ion storage. The preserved electrode architecture, underscoring the robustness of its porous network, explains the superior cycling stability and capacity retention of CBW16 compared to CBW14. Overall, post-cycling SEM and Raman analyses confirmed that the capacity decay observed in the case of CBW14 originates from the electrode matrix amorphisation.

A well-connected porous network, as observed in CBW16, ensures both efficient ion diffusion and structural robustness. While micropores provide extensive surface area for charge storage, they are highly susceptible to mechanical stress during repeated charge–discharge cycles, leading to pore collapse, crack formation, and blocked ion transport pathways, as exemplified by the micropore-rich CBW14 electrode.[67,68] The limited mesopore volume in CBW14 further restricts ion transport, thereby reducing the effective surface area accessible for electrochemical reactions. In contrast, CBW18, with higher mesopore content than CBW16, demonstrates that mesopores alone cannot ensure high capacity. These findings underscore the importance of achieving an optimal pore size distribution, where micropores contribute to charge storage and mesopores facilitate ion transport while mitigating structural degradation. By tuning the biomass/KOH activation ratio, it is possible to engineer a hierarchical pore structure that maximizes accessible surface area while minimizing diffusion resistance. This balance, exemplified by CBW16, is key to developing activated carbon electrodes with both high energy density and superior cycling stability for aluminum battery systems.

4. Conclusion

Birch wood-derived activated carbons (CBWs) prepared via carbonization at 900 °C and KOH activation under N_2 have been shown to offer a synergistic combination of textural and electrochemical properties for aluminum battery cathodes. Among the samples studied, CBW16 (biochar: KOH = 1 : 6) exhibited the most favorable pore architecture, high BET surface area (3306 m^2 g^{-1}), large total pore volume, and a balanced micro-mesopore network that translated into exceptional battery performance. In an $AlCl_3$:[EMIM]Cl ionic liquid electrolyte (0.01–2.2 V), CBW16 delivered a discharge capacity of $\approx$140 mAh g^{-1} at 0.1 A g^{-1}, retained 86 mAh g^{-1} after 5700 cycles at 1 A g^{-1}, and achieved energy densities of 155 Wh kg^{-1} (0.1 A g^{-1}) and 95 Wh kg^{-1} (1 A g^{-1}). These results surpass both CBW14 and CBW18, and many reported biomass-derived and synthetic carbon cathodes, underscoring the critical role of hierarchical porosity in enabling high reversible capacity, rapid ion transport, and long-term stability. Furthermore, the use of an abundant, low-cost biomass precursor and a straightforward activation protocol highlight the scalability and economic viability of CBW16 for large-scale energy storage. Overall, this work demonstrates that optimizing KOH activation levels to achieve a balanced pore structure is key to unlocking the full potential of carbon cathodes in next-generation aluminum batteries.

Conflict of Interest

The authors declare no conflict of interest.

Data Availability Statement

The data that support the findings of this study are available from the corresponding author upon reasonable request.

Batteries & Supercaps

Research Article
doi.org/10.1002/batt.202500779

Chemistry Europe
European Chemical
Societies Publishing

[1] Z. Hu, H. Zhang, H. Wang, F. Zhang, Q. Li, H. Li, *ACS Mater. Lett.* **2020**, *2*, 887.

[2] T. Dutta, J. M. Gladis, *J. Energy Storage* **2024**, *86*, 111287.

[3] P. Thanwisai, N. Chaiyapo, P. Phuenhinlad, Y. Kanaphan, J. Nash, C. Chotsuwan, A. Klamchuen, Y. Wang, T. Nann, N. Meethong, *Carbon* **2022**, *191*, 195.

[4] N. Melzack, R. G. A. Wills, *Front. Chem. Eng* **2022**, *4*, 2022.

[5] X. Yang, C. Huang, *J. Energy Storage* **2024**, *78*, 110069.

[6] G. A. Elia, K. V. Kravchyk, M. V. Kovalenko, J. Chacón, A. Holland, R. G. A. Wills, *J. Power Sources* **2021**, *481*, 228870.

[7] F. A. Kayakool, H. Pant, M. Paul, G. S. D. Reis, G. Manavalan, V. V. S. S. Srikanth, M. Thyrel, S. Petnikota, *Carbon Resour. Convers.* **2025**, *8*, 100301.

[8] M. Paul, A. Grimm, G. S.ões D. Reis, G. Manavalan, S. S. E., M. Thyrel, S. Petnikota, *ChemElectroChem* **2025**, *12*, e202400549.

[9] S. Petnikota, R. Chua, K. M. Boopathi, R. Satish, F. Bonaccorso, V. Pellegrini, M. Srinivasan, *J. Electrochem. Soc.* **2020**, *167*, 100514.

[10] S. Petnikota, D. Koch, M. Imran, J. Buha, J. K. Panda, M. A. Garakani, L. Marasco, A. Gamucci, F. Bonaccorso, V. Pellegrini, *Sustainable Energy Fuels* **2022**, *6*, 4311.

[11] S. Petnikota, G. S.ões D. Reis, F. A. Kayakool, V. S. S. S. Vadali, J. Välikangas, U. Lassi, M. Thyrel, *ACS Appl. Energy Mater.* **2024**, *7*, 6862.

[12] G. S. Reis, S. Petnikota, C. M. Subramaniyam, H. P. de Oliveira, S. Larsson, M. Thyrel, U. Lassi, F. García Alvarado, *Nanomaterials* **2023**, *13*, 765.

[13] S. K. Das, S. Mahapatra, H. Lahan, *J. Mater. Chem. A* **2017**, *5*, 6347.

[14] M.-C. Lin, M. Gong, B. Lu, Y. Wu, D.-Y. Wang, M. Guan, M. Angell, C. Chen, J. Yang, B.-J. Hwang, H. Dai, *Nature* **2015**, *520*, 324.

[15] R. D. McKerracher, A. Holland, A. Cruden, R. G. A. Wills, *Carbon* **2019**, *144*, 333.

[16] H. Huang, F. Zhou, P. Lu, X. Li, P. Das, X. Feng, K. Müllen, Z.-S. Wu, *Energy Storage Mater.* **2020**, *27*, 396.

[17] S. Zhao, H. Chen, J. Li, J. Zhang, *New J. Chem.* **2019**, *43*, 15014.

[18] Z. Liu, J. Wang, X. Jia, W. Li, Q. Zhang, L. Fan, H. Ding, H. Yang, X. Yu, X. Li, B. Lu, *ACS Nano* **2019**, *13*, 10631.

[19] J. Li, Q. Liu, R. A. Flores, J. Lemmon, T. Bligaard, *Phys. Chem. Chem. Phys.* **2020**, *22*, 5969.

[20] W. Yang, H. Lu, Y. Cao, B. Xu, Y. Deng, W. Cai, *ACS Sustainable Chem. Eng.* **2019**, *7*, 4861.

[21] L. Geng, J. P. Scheifers, C. Fu, J. Zhang, B. P. T. Fokwa, J. Guo, *ACS Appl. Mater. Interfaces* **2017**, *9*, 21251.

[22] Z. Hu, K. Zhi, Q. Li, Z. Zhao, H. Liang, X. Liu, J. Huang, C. Zhang, H. Li, X. Guo, *J. Power Sources* **2019**, *440*, 227147.

[23] X. Wen, Y. Liu, A. Jadhav, J. Zhang, D. Borchardt, J. Shi, B. M. Wong, B. Sanyal, R. J. Messinger, J. Guo, *Chem. Mater.* **2019**, *31*, 7238.

[24] Z. Li, J. Li, F. Kang, *Electrochim. Acta* **2019**, *298*, 288.

[25] K. Zhang, T. H. Lee, B. Bubach, H. W. Jang, M. Ostadhassan, J.-W. Choi, M. Shokouhimehr, *Sci. Rep.* **2019**, *9*, 13665.

[26] M. Walter, K. V. Kravchyk, C. Böfer, R. Widmer, M. V. Kovalenko, *Adv. Mater.* **2018**, *30*, 1705644.

[27] J. Li, J. K. El-Demellawi, G. Sheng, B. Björk, F. Zeng, J. Zhou, J. Liao, J. Wu, J. Rosen, X. Liu, H. N. Alshareef, S. Tu, *Energy Environ. Mater.* **2024**, *7*, e12733.

[28] I. Ashurov, S. Iskandarov, U. Khalilov, K. Ashurov, *Appl. Sol. Energy* **2022**, *58*, 334.

[29] C. Zhang, R. He, J. Zhang, Y. Hu, Z. Wang, X. Jin, *ACS Appl. Mater. Interfaces* **2018**, *10*, 26510.

[30] P. Thanwisai, P. Phuenhinlad, N. Chaiyapo, Y. Kanaphan, J. Nash, C. Chotsuwan, T. Rattana-amron, A. Klamchuen, N. Meethong, *J. Phys.: Conf. Ser.* **2021**, *1719*, 012059.

[31] A. R. Selvaraj, D. Chinnadurai, I. Cho, J.-S. Bak, K. Prabakar, *J. Energy Storage* **2022**, *52*, 104928.

[32] S. Yang, S. Wang, X. Liu, L. Li, *Carbon* **2019**, *147*, 540.

[33] P. Pietrzyk-Thel, A. Jain, M. Osial, K. Sobczak, M. Michalska, *Electrochim. Acta* **2025**, *525*, 146129.

[34] S. Sahoo, T. Nagaraja, M. Michalska, S. R. Das, *Nanoscale Adv.* **2025**, *7*, 3331.

[35] S. R. Manippady, M. Michalska, M. Krajewski, K. Bochenek, M. Basista, A. Zaszczynska, T. Czeppe, L. Rogal, A. Jain, *Mater. Sci. Eng. B* **2023**, *297*, 116766.

[36] H. Krishnamoorthy, R. Ramyea, A. Maruthu, K. Kandasamy, M. Michalska, S. K. Kandasamy, *Bioresour. Technol. Rep.* **2022**, *19*, 101187.

[37] A. Jain, M. Ghosh, M. Krajewski, S. Kurungot, M. Michalska, *J. Energy Storage* **2021**, *34*, 102178.

[38] J. Phiri, J. Dou, T. Vuorinen, P. A. C. Gane, T. C. Maloney, *ACS Omega* **2019**, *4*, 18108.

[39] Y. Li, J. Mei, L. Wu, Q. Xu, Z. Li, *Int. J. Hydrogen Energy* **2024**, *49*, 67.

[40] L. L. Zhang, X. Zhao, M. D. Stoller, Y. Zhu, H. Ji, S. Murali, Y. Wu, S. Perales, B. Clevenger, R. S. Ruoff, *Nano Lett.* **2012**, *12*, 1806.

[41] Y. Zhu, S. Murali, M. D. Stoller, K. J. Ganesh, W. Cai, P. J. Ferreira, A. Pirkle, R. M. Wallace, K. A. Cychosz, M. Thommes, D. Su, E. A. Stach, R. S. Ruoff, *Science* **2011**, *332*, 1537.

[42] A. Iakunkov, V. Skrypnychuk, A. Nordenström, E. A. Shilayeva, M. Korobov, M. Prodana, M. Enachescu, S. H. Larsson, A. V.Talyzin, *Phys. Chem. Chem. Phys* **2019**, *21*, 17901.

[43] A. Nordenström, N. Boulanger, A. Iakunkov, G. Li, R. Mysyk, G. Bracciale, P. Bondavalli, A. V. Talyzin, *Nanoscale Adv.* **2022**, *4*, 4689.

[44] G. Li, A. iakunkov, N. Boulanger, O. A. Lazar, M. Enachescu, A. Grimm, A. V. Talyzin, *RSC Adv.* **2023**, *13*, 14543.

[45] A. V. T. Boulanger, S. Xiong, M. Hultberg, A. Grimm, *Colloids Surf. A* **2024**, *680*, 132684.

[46] Y. Lv, F. Zhang, Y. Dou, Y. Zhai, J. Wang, H. Liu, Y. Xia, B. Tu, D. Zhao, *J. Mater. Chem.* **2012**, *22*, 93.

[47] S. C. Grimm, F. G. Gentili, J.-P. Mikkola, T. Hu, U. Lassi, L. F. O. Silva, E. C. Lima, G. S. dos Reis, *Colloids Surf., A* **2025**, *713*, 136486.

[48] S. S.E., A. Grimm, M. Paul, C. T. Cherian, M. Thyrel, P. Molaiyan, U. Lassi, S. Petnikota, G. S. D. Reis, *Chem. Eng. J. Adv.* **2025**, *22*, 100762.

[49] P. Liu, S. Sun, S. Huang, Y. Wu, X. Li, X. Wei, S. Wu, *Catalysts* **2024**, *14*, 814.

[50] P. Molaiyan, S. E. Mailhiot, K. Voges, A. M. Kantola, T. Hu, P. Michalowski, A. Kwade, V.-V. Telkki, U. Lassi, *Mater. Des.* **2023**, *227*, 111690.

[51] Y. Ji, T. Li, L. Zhu, X. Wang, Q. Lin, *Appl. Surf. Sci.* **2007**, *254*, 506.

[52] O. Oginni, K. Singh, G. Oporto, B. Dawson-Andoh, L. McDonald, E. Sabolsky, *Bioresour. Technol. Rep.* **2019**, *7*, 100266.

[53] W. Chen, M. Gong, K. Li, M. Xia, Z. Chen, H. Xiao, Y. Fang, Y. Chen, H. Yang, H. Chen, *Appl. Energy* **2020**, *278*, 115730.

[54] P. B. Naik, P. Thippeswamy, R. Nagaraj, R. Puttaswamy, H. K. Beere, U. N. Maiti, C. Mondal, N. S. Kotrappanavar, D. Ghosh, *ACS Sustainable Chem. Eng* **2022**, *10*, 1471.

[55] H. Wang, X. Liu, P. Niu, S. Wang, J. Shi, L. Li, *Matter* **2020**, *2*, 1377.

[56] J. i. Hayashi, A. Kazehaya, K. Muroyama, A. P. Watkinson, *Carbon* **2000**, *38*, 1873.

[57] R. Serfling, *North Am. Actuarial J.* **2002**, *6*, 95.

[58] M. Jerigová, M. Odziomek, N. López-Salas, *ACS Omega* **2022**, *7*, 11544.

[59] A. Farooq, L. Reinert, J.-M. Levêque, N. Papaiconomou, N. Irfan, L. Duclaux, *Microporous Mesoporous Mater.* **2012**, *158*, 55.

[60] R. M. Carvalho, L. M. N. B. F. Santos, M. Bastos, J. C. S. Costa, *Langmuir* **2024**, *40*, 3949.

[61] S. Petnikota, H. Maseed, V. V. S. S. Srikanth, M. V. Reddy, S. Adams, M. Srinivasan, B. V. R. Chowdari, *J. Phys. Chem. C* **2017**, *121*, 3778.

[62] S. Petnikota, N. K. Rotte, M. V. Reddy, V. V. S. S. Srikanth, B. V. R. Chowdari, *ACS Appl. Mater. Interfaces* **2015**, *7*, 2301.

[63] S. Petnikota, N. K. Rotte, V. V. S. S. Srikanth, B. S. R. Kota, M. V. Reddy, K. P. Loh, B. V. R. Chowdari, *J. Solid State Electrochem.* **2014**, *18*, 941.

[64] C. Li, P. C. Rath, S.-X. Lu, J. Patra, C.-Y. Su, D. Bresser, S. Passerini, J.-K. Chang, *Chem. Eng. J.* **2021**, *417*, 129131.

[65] O. E. Eleri, F. Huld, J. Pires, W. M. Tucho, P. Schweigart, A. M. Svensson, F. Lou, Z. Yu, *Electrochim. Acta* **2023**, *453*, 142359.

[66] S. Petnikota, G. D. Reis, F. A. L. I. Kayakool, V. V. S. S. Srikanth, J. Välikangas, U. Lassi, M. Thyrel, *ECS Meeting Abstr.* **2023**, *MA2023*, 3328.

[67] N. M. Thazin, N. Chaiammart, M. M. Thu, G. Panomsuwan, *J. Met., Mater. Min.* **2022**, *32*, 55.

[68] Y. Wang, Y. Chen, H. Zhao, L. Li, D. Ju, C. Wang, B. An, *Nanomaterials* **2022**, *12*, 3804.